

# We are IntechOpen, the world's leading publisher of Open Access books Built by scientists, for scientists

6,900

Open access books available

186,000

International authors and editors

200M

Downloads

Our authors are among the

154

Countries delivered to

TOP 1%

most cited scientists

12.2%

Contributors from top 500 universities



WEB OF SCIENCE™

Selection of our books indexed in the Book Citation Index  
in Web of Science™ Core Collection (BKCI)

Interested in publishing with us?  
Contact [book.department@intechopen.com](mailto:book.department@intechopen.com)

Numbers displayed above are based on latest data collected.  
For more information visit [www.intechopen.com](http://www.intechopen.com)



---

# Mathematical Modelling and Numerical Investigations on the Coanda Effect

---

A. Dumitrache, F. Frunzulica and T.C. Ionescu

Additional information is available at the end of the chapter

<http://dx.doi.org/10.5772/50403>

---

## 1. Introduction

Jets are frequently observed to adhere to and to flow around nearby solid boundaries. This general class of phenomena, which may be observed in both liquid and gaseous jets, are known as the Coanda effect. Flows deflected by a curved surface have caused great interest in last fifty years [1-4]. A major interest in the study of this phenomenon is caused by the possibility of using this effect to aircrafts with short takeoff and landing, for fluidic vectoring.

Flow control offers a multitude of opportunities for improving not only the aerodynamic performance, but also the safety and environmental impact of flight vehicles. Circulation control (CC) is one type of flow control which is currently receiving considerable attention. Such flow control is usually implemented by tangentially injecting a jet sheet over a rounded wing trailing edge. The jet sheet remains attached further along the curved surface of the wing due to the Coanda effect (i.e., a balance of pressure and centrifugal forces). This results in the effective camber of the wing being increased, producing lift augmentation.

At the beginning of the chapter we achieve an analytic solution that approximates a two-dimensional Coanda flow. The validity of the results is limited to cases  $b/R \ll 1$ , since in the tangential component of the momentum equation, the curvature was neglected ( $y^* \ll 1$ ).

In many applications that use boundary layer control by tangential blowing, the solid surface downstream of the blowing slot is strongly curved and, in this case, the prediction of the jet involves both separation and a more accurate knowledge of the flow (radial and tangential pressure - velocity profiles) which can be done by CFD methods.

After the analytical approach, using the FLUENT code both external and internal flows are analyzed, with emphasis on the Coanda effect, in order to determine its advantages and limitations. Finally, we analyze the situations when bifurcations of the flow occur.

---

## 2. Similar solution for a Coanda flow

Jets are frequently observed to adhere to and flow round nearby solid boundaries. This general class of phenomena, which may be observed in both liquid and gaseous jets, is known as the Coanda effect. In recent years, great interest has been taken in flows deflected by a curved surface. Studying this phenomenon is very important due to the possibility of using the Coanda effect to aircrafts with short takeoff and landing, for fluidic vectoring.

This section deals with the steady two-dimensional, laminar and turbulent flow of an incompressible fluid that develops like a jet-sheet on a cylinder surface, i.e., a Coanda flow [5]. We show that this flow can be approximated well enough by similar solutions for both the laminar and the turbulent regime. Basically we use Falkner-Skan transformations of the momentum equations that can be reduced to one ordinary differential equation (ODE). These solutions are presented in this section for both the laminar and the turbulent flow. The results are given in the form of analytical expressions for the mass flow, thrust and jet-sheet thickness depending on the angle of deviation.

We also consider the possibility of the thrust augmentation yielded by the fluid entrainment of the jet flow. Thrust vectoring of aircraft which is the key technology for current and future air vehicles, can be achieved by utilizing the Coanda effect to alter the angle of the primary jet from an engine exhaust nozzle. Furthermore, the increased entrainment by the Coanda surface coupled with the primary jet fluid can augment the thrust, see e.g., [6].

The problem considered here is only a crude approximation of the physical phenomenon. However, we believe that the singular solutions that we develop pave the way towards a further, more accurate approach of the problem.

### 2.1. Mathematical model

Let us consider the steady two-dimensional flow of an incompressible fluid developed on a cylindrical surface like a jet-sheet. The boundary-layer type equations are written in a curvilinear coordinate system shown in Figure 1. Assuming that the width of the jet slot is small compared to the curvature radius of the cylinder,  $R$ , the boundary-layer approximations can be applied yielding the simplified equations of motion

$$\frac{1}{r} \frac{\partial V_\theta}{\partial \theta} + \frac{\partial V_r}{\partial r} + \frac{V_r}{r} = 0, \quad (1)$$

$$V_r \cdot \frac{\partial V_\theta}{\partial r} + \frac{V_\theta}{r} \cdot \frac{\partial V_\theta}{\partial \theta} = \frac{1}{\rho} \cdot \frac{\partial \tau}{\partial r}, \quad (2)$$

$$\rho \frac{V_\theta^2}{r} = \frac{\partial p}{\partial r}, \quad (3)$$

where the laminar shear stress is  $\tau = \mu \frac{\partial V_\theta}{\partial r}$  and the turbulent shear stress, where the contribution of the laminar sublayer is neglected (omit the term  $\mu \frac{\partial V_\theta}{\partial r}$ ), has the form  $\tau = \mu_t \frac{\partial V_\theta}{\partial r}$ , with  $\mu_t$  the turbulent viscosity, assumed constant in a cross-section like shear layer, i.e.,  $\nu_t / \nu = \sigma \theta^c$ .

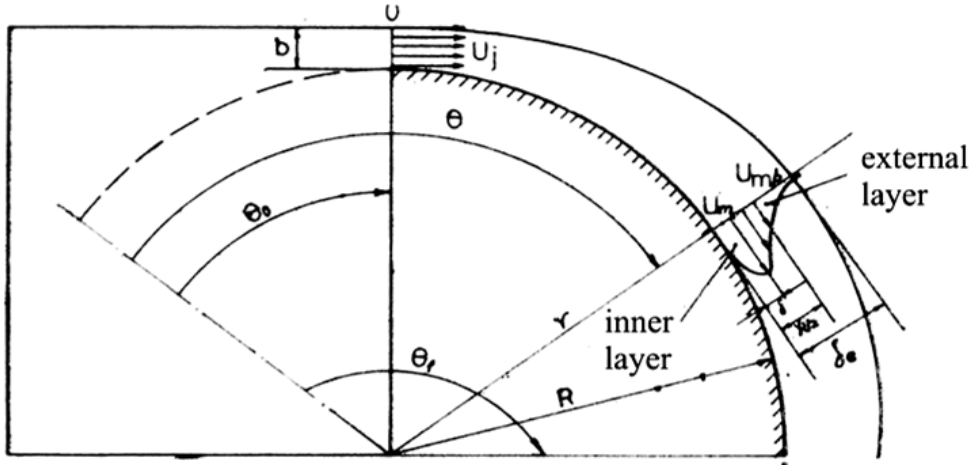


**Figure 1.** Coordinate system and notation.

The variables in equations (1)-(3) can be made dimensionless, as follows

$$V_r^* = \frac{V_r}{U_j}, V_\theta^* = \frac{V_\theta}{U_j}, r^* = \frac{r}{R}, p^* = \frac{P}{\rho U_j^2}, Re = \frac{U_j R}{\nu}, y^* = \frac{y}{R} = r^* - 1, \nu = \mu / \rho, y^* \ll 1,$$

where  $U_j$  is the velocity of the jet at the exit of nozzle ( $\theta = \theta_0$ ) (assumed constant in cross-section),  $Re$  is the Reynolds number based on the cylinder radius and  $y$  is the radial distance from the cylinder surface, i.e.,  $r = R$ .

The dimensionless continuity equation (1) is satisfied by a stream function, chosen such that  $V_r^* = \left(-\frac{1}{r^*}\right) (\partial \psi / \partial \theta)$  and  $V_\theta^* = \frac{\partial \psi}{\partial r^*}$ . Since  $y^*$  is much smaller than the unity, it may be neglected compared with the unity in the dimensionless equation (2). Introducing a modelling variable of the form

$$\eta = Re \cdot y^* \cdot \frac{c+1}{\sigma} \theta^{(c+1)(a-1)} \quad (4)$$

and with the stream function chosen as

$$\psi = \theta^{a(c+1)} f(\eta), \quad (5)$$

equation (2) can be transformed into the following nonlinear ordinary differential equation:

$$f''' + a f f' + (1 - 2a) f'^2 = 0. \tag{6}$$

The choice of the constant  $a$  depends on the boundary conditions. By definition,

$$V_r^* = -\frac{1}{r^*} \cdot \frac{d\psi}{d\theta} \cong -\theta^{a(c+1)-1} [a(c+1)f + (c+1)(a-1)\eta f'],$$

$$V_\theta^* = \frac{\partial\psi}{\partial r^*} = \frac{\partial\psi}{\partial y^*} = \text{Re} \frac{c+1}{\sigma} \theta^{(c+1)(2a-1)} f'.$$

Integrating equation (6) easily proves that the values  $a = 1/3$  and  $a = 1/2$  satisfy the boundary conditions of the free jet flow case and of the boundary layer on a flat plate with zero incident, respectively. For the Coanda type flow considered here, the boundary conditions attached to equation (6) are

$$\eta = 0; f = 0, f'(0) = 0, \text{ (non-slip condition),}$$

$$\eta \rightarrow \infty: f' = 0, f'' = 0, \text{ (condition at the edge).}$$

Integrating equation (6) from  $\eta$  to  $\infty$ , with the above conditions, yields

$$-f'' - a f f' + (1 - 3a) \int_{\eta}^{\infty} f'^2 d\eta = 0. \tag{7}$$

Further integrating equation (7) by means of the integrant factor  $f'$ , yields:

$$\frac{1}{2} f'^2 - a f \int_{\eta}^{\infty} f'^2 d\eta + (1 - 4a) \int_{\eta}^{\infty} g f' d\eta = 0, \tag{8}$$

where  $g(\eta) = \int_{\eta}^{\infty} f'^2 d\eta$ .

Equation (8) written at the wall, i.e.,  $\eta = 0$ , leads to  $(1 - 4a) \int_0^{\infty} g f' d\eta = 0$ . Since  $\int_0^{\infty} g f' d\eta \neq 0$ ,

then either  $(1 - 4a) = 0$ , or  $a = 1/4$ . This value satisfies the boundary conditions for the Coanda flow. Thus, the velocity components can be written as

$$V_r^* = -\frac{c+1}{4} \theta^{\frac{c+1}{4}-1} [1 - 3\eta f'], \tag{9}$$

$$V_\theta^* = \text{Re} \frac{c+1}{\sigma} \theta^{-\frac{c+1}{2}} f'. \tag{10}$$

Hence, equation (6) is integrated for the value  $a$  corresponding to the Coanda flow. Writing equation (6) with  $a = 1/4$  yields

$$f''' + \frac{1}{4} f f'' + \frac{1}{2} f'^2 = 0. \quad (11)$$

Successively integrating equation (11) with the integrant factors  $f$  and  $f^{-3/2}$  and taking into account the appropriate boundary conditions firstly gives  $f'' f + \frac{1}{4} f' f^2 - \frac{1}{2} f'^2 = 0$  and then

$$6f' + f^2 = f_\infty^{3/2} f^{1/2}, \quad (12)$$

where  $f_\infty = \lim_{\eta \rightarrow \infty} f$ . Choosing  $F = (f / f_\infty)^{1/2}$  equation (12) becomes an equation with separable variables whose solution is written as

$$\eta f_\infty = 4\sqrt{3} \operatorname{actg} \left( \frac{\sqrt{3}F}{2+F} \right) + 2 \ln \frac{F^2 + F + 1}{(F-1)^2}. \quad (13)$$

Thus, the quantities  $\eta$  and  $f$  can be expressed as explicit functions of the parameter  $F$  and so  $f$  becomes

$$f = f_\infty F^2. \quad (14)$$

We further obtain explicit relations of  $F$  for the quantities  $f'$ ,  $f''$ ,  $f'''$  as follows:

$$f' = \frac{f_\infty^2}{6} (F - F^4), \quad (15)$$

$$f'' = \frac{f_\infty^3}{72} (1 - F^3)(1 - 4F^3), \quad (16)$$

$$f''' = -\frac{f_\infty^4}{288} F^2 (1 - F^3)(5 - 8F^3). \quad (17)$$

The domain of values of  $F$  is from  $[0, 1]$ , hence the independent variable  $\eta$  ranges from 0 to  $\infty, \eta \in [0, \infty)$ .

Thus, the problem is completely determined and the solution of equation (11) with given boundary conditions is represented by equations (13)-(17). Calculated values of  $\eta f_\infty$ ,  $f / f_\infty$ ,  $f' / f_\infty^2$ ,  $f'' / f_\infty^3$  and  $f''' / f_\infty^4$  are presented in Figure 2

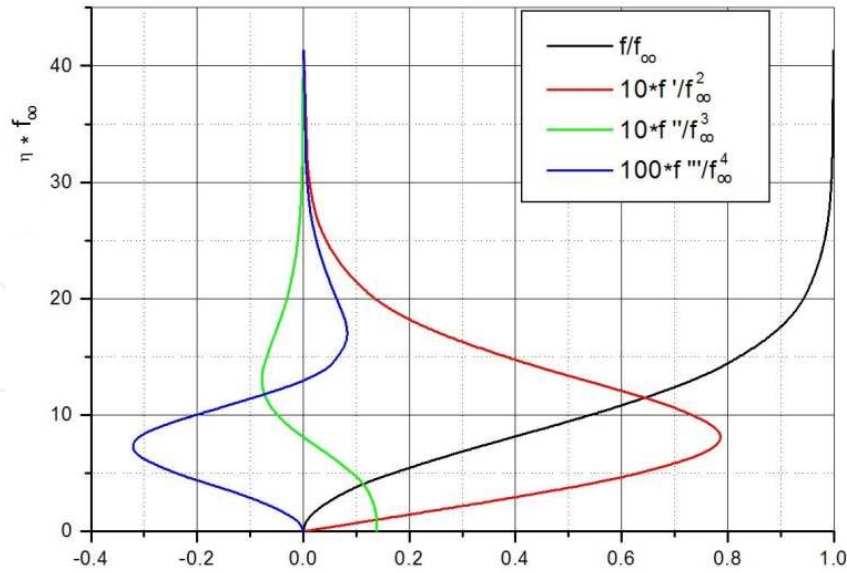


Figure 2. Variations of terms for the similar solution.

### 2.2. Results

**Laminar flow.** Since for a laminar flow,  $\mu_t / \mu = 1$ , then  $\sigma = 1$  and  $c = 0$ . So, the components of the velocity become

$$V_r^* = -\frac{\theta^{-3/4}}{4} [f - 3\eta f'], \tag{18}$$

$$V_\theta^* = \text{Re} \theta^{-1/2} f'. \tag{19}$$

If the mass flow and the momentum of the jet are given at output ( $\theta = \theta_0$ ) then we are able to compute the value of  $\theta_0$ . Since the boundary layer approximations are not valid near the origin of the jet, this value should be regarded as a virtual origin of the similar motion. Considering the mass flow per length unity of the slot  $Q_m = \rho U_j b$ , and  $b$  the width of the slot, then

$$Q_m = \rho U_j b = \int_0^\infty \rho V_\theta dy|_{\theta_0} = \rho U_j R \theta_0^{1/4} f_\infty,$$

or

$$\theta^{1/4} = \left(\frac{b}{R}\right) \frac{1}{f_\infty}. \tag{20}$$

Now, let the momentum of the jet in the slot be  $\rho U_j^2 b = Q_m U_j$ . This assumption holds if the velocity does not depend on the length of the slot. This contradicts the assumption that the flows are similar at  $\theta = \theta_0$ . The jet model is similar to the material point model of solid

mechanics, where only the physical size of the body (mass) is taken into account. According to this model, the theoretical jet with given momentum comes out from a zero width slot at  $\theta = 0$  and achieves its mass flow in similar flow conditions at  $\theta = \theta_0$ . At the origin  $\theta = 0$ , the flow is singular. Equating the momentum of the physical jet with the one theoretically determined at  $\theta = \theta_0$  yields  $\rho U_j^2 b = \int_0^{\theta_0} \rho V_\theta^2 dy|_{\theta_0}$  and further

$$b = R \frac{\text{Re}}{\theta_0^{1/4}} \int_0^\infty f'^2 d\eta. \quad (21)$$

The integral from equation (21) is easily computed yielding

$$\frac{b}{R} = \frac{\text{Re}}{Q_0^{1/4}} \cdot \frac{f_\infty^3}{18}. \quad (22)$$

Substituting  $f_\infty$  from (20) into (22) leads to

$$\theta_0 = \left( \frac{b}{R} \right)^2 \frac{\text{Re}}{18}. \quad (23)$$

Thus,  $f_\infty$  that does not appear in the expression of  $\theta_0$ , depends only on the curvature wall and the jet characteristics, i.e.,

$$f_\infty = \left( \frac{b}{R} \right)^{1/2} \left( \frac{18}{\text{Re}} \right)^{1/4}. \quad (24)$$

This means that  $f_\infty$  is a curvature parameter. In [7] an entrainment parameter  $A$  has been defined as a measure of the fluid amount involved in flow. The fluid entrainment is an important physical process because it determines the extent of the attachment region of the Coanda effect. The entrainment parameter is defined by

$$A = \frac{1}{U_j} \cdot \frac{d}{R d\theta} \int_0^\infty V_\theta dy. \quad (25)$$

For the laminar flow, we obtain the dimensionless entrainment parameter as

$$A = \frac{f_\infty}{4} \cdot \theta^{-3/4}, \quad (26)$$

which shows that the entrainment attains its maximum at the jet origin.

Next, we calculate the thrust produced by the deflection of the jet with  $90^\circ$ . If  $F_t$  is the

thrust per width unity, then  $F_t = \int_0^\infty \rho V_\theta^2 dy|_{\theta=\theta_1} + \int_0^\infty (p - p_\infty) dy|_{\theta=\theta_1}$ , where the first term

represents the flow of the momentum and  $\theta_1 = \theta_0 + 90^\circ$ . Integrating equation (3) yields

$$p_\infty - p = \int_r^\infty \rho V_\theta^2 \frac{dr}{r} = \int_{y^*}^\infty \frac{\rho U_j^2 V_\theta^{*2}}{1 + y^*} dy^*.$$

Since  $y^*$  is much smaller compared to the unity, we may neglect it in the denominator.

Hence, the integral becomes  $\int_\eta^\infty \rho U_j^2 \text{Re} \theta^{-1/4} f'^2 d\eta$ , which leads to

$$p_\infty - p = \rho U_j^2 \text{Re} \frac{f_\infty^3}{18\theta^{1/4}} (1 - F^3)^2.$$

Integrating once, we obtain the second term, which is the contribution of pressure, i.e.,

$$\int_0^\infty (p - p_\infty) dy \Big|_{\theta=\theta_1} = \frac{\rho U_j^2}{2} R \theta_1^{1/2} f_\infty^2.$$

As the total momentum flux is  $\rho U_j^2 R \text{Re} \theta_1^{-1/4} \frac{f_\infty^3}{18}$ , the expression of thrust force becomes

$$F_t = \rho U_j^2 R f_\infty^2 \left[ \frac{\text{Re} f_\infty}{18 \theta^{1/4}} - \frac{\theta_1^{1/2}}{2} \right]. \quad (27)$$

By comparison with the non-deflected free jet, we introduce an enhancement factor of thrust defined by the ratio

$$T = \frac{F_t \Big|_{\theta=\theta_1}}{F_t \Big|_{\theta=\theta_0}} = \frac{F_t}{\rho U_j^2 b} = \frac{R}{b} \theta_1^{-1/4} \left[ \frac{\text{Re} f_\infty}{18} - \frac{f_\infty^2 \theta_1^{3/4}}{2} \right]. \quad (28)$$

Using equations (22), (23) and (24),  $T$  becomes

$$T = \left( \frac{\theta_0}{\theta_1} \right)^{1/4} - \frac{1}{2} \left[ \frac{9\pi}{\text{Re}} + \left( \frac{b}{R} \right)^2 \right]^{1/2}. \quad (29)$$

Since  $\theta_1 = \theta_0 + \pi/2$ ,  $9\pi/\text{Re} \ll 1$  and  $\left(\frac{b}{R}\right)^2 \ll 1$ , one finds that  $T < 1$ , i.e., for the considered case there is no thrust increase, but only a change in its direction.

It defines the finite thickness of the jet sheet,  $\delta$ , the same as the boundary layer, namely the

value of  $y$  where the section  $\theta > \theta_0$  has  $\frac{V_\theta}{V_{\theta_{\max}}} = 0.01$ .

Since  $V_\theta^* = \frac{V_\theta}{U_j} = \text{Re} \cdot f'^{1/2}$ ,  $\frac{V_\theta}{V_{\theta \max}} = \frac{V_\theta^*}{V_{\theta \max}^*} = \frac{f'}{f'_{\max}}$  the problem is to find the value of  $\eta$  for

which  $f' / f'_{\max} = 0.01$ . By equation (15),  $f'_{\max} = (f_\infty^2 / 8)^{1/3}$  implying that

$f' / f'_{\max} = \frac{4^{4/3}}{3} (F - F^4)$ . For  $f' / f'_{\max} = 0.01$  it follows that  $F = 0.998421$  and by equation

(13), we have  $\eta f_\infty = 31.622$ . Substituting these values in (4) finally yields  $\delta^* = \frac{31,622}{\text{Re} f_\infty} \theta^{3/4}$ ,

where the angle  $\theta$  is measured from the apparent origin (the point of zero sheet thickness).

Denoting by  $x = R\theta$  the distance along the cylinder surface, one notices that  $\delta^* \sim x^{3/4}$  and  $V_{\theta \max}^* \sim x^{-1/2}$ .

**Turbulent flow.** For turbulent flows it is first necessary to determine the eddy viscosity  $\mu_t$ . Wall jets are important test cases for turbulence models because they contain a boundary-layer near the wall which interacts with a free shear layer (Figure 3). Thus, they grow much less than free jets. This reduction in the wall jet development is mainly due to the presence of the wall surface where the entrainment by the jet is inhibited on the side nearest to the surface. The velocity fluctuation damping is transmitted to the outer layer and, since the transfer of side momentum component is closely related to the side component of velocity fluctuations, the shear stress and the development of the jet are reduced. Conversely, a relatively high turbulence degree of the outer layer of the wall jet has an effect similar to the turbulence of free jet in the boundary layer case. Usually, the models of turbulence based on turbulent viscosity do not take into account the jet damping at the side wall and in this way, the empirical constants used for the free jet overestimate the development of the jet wall. For example, the  $k - \varepsilon$  model with standard constants, given in [8], yields values of the width of the jet augmented by 30 %. Turbulence models based on the shear stress transport equations (6) can correctly predict the wall jet, with standard constants, only if the equations take into account the wall effect on the correlation pressure – strain velocity, see [8], [9]. If this influence is not taken into account the models yield 20% higher values. Use of the turbulence models based on transport equations is however complex and expensive. Hence, in this section (for analytical solution) we are limited to a simple algebraic model, of turbulent viscosity type, which estimates accurately enough the main features of the considered Coanda flow.

We assume that the turbulent viscosity for a moderate curvature of the flow is governed by the same laws as in the case without curvature. Hence

$$\nu_t = K \cdot V_{\theta m} \cdot y_{1/2} = \nu K \text{Re} V_{\theta m}^* y_{1/2}^* \quad (30)$$

where  $V_{\theta m}$  is the maximum speed of flow,  $y_{1/2}$  is the point of the outer layer where  $\frac{V_\theta}{V_{\theta m}} = \frac{1}{2}$ ,

and the mixing coefficient  $K$  is an empirical constant, same as in the case without curvature.

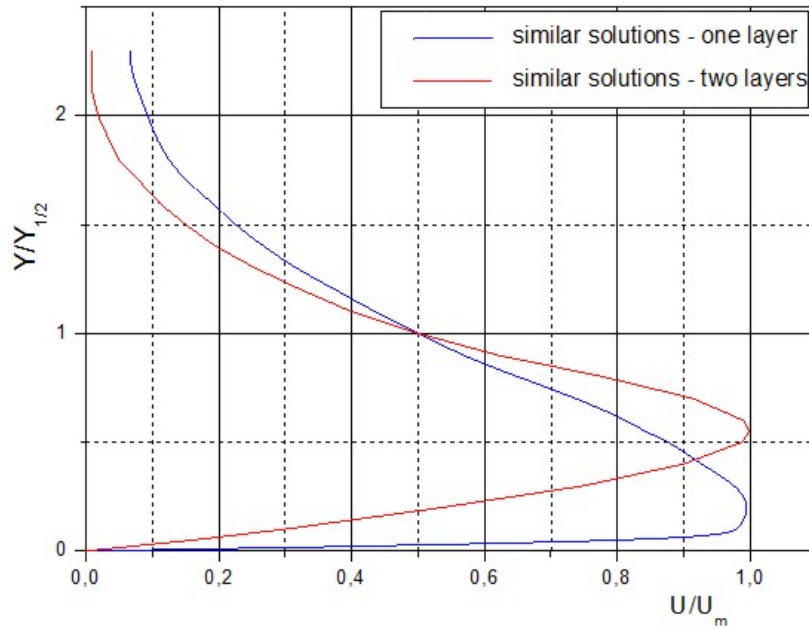


Figure 3. Similar velocity profiles.

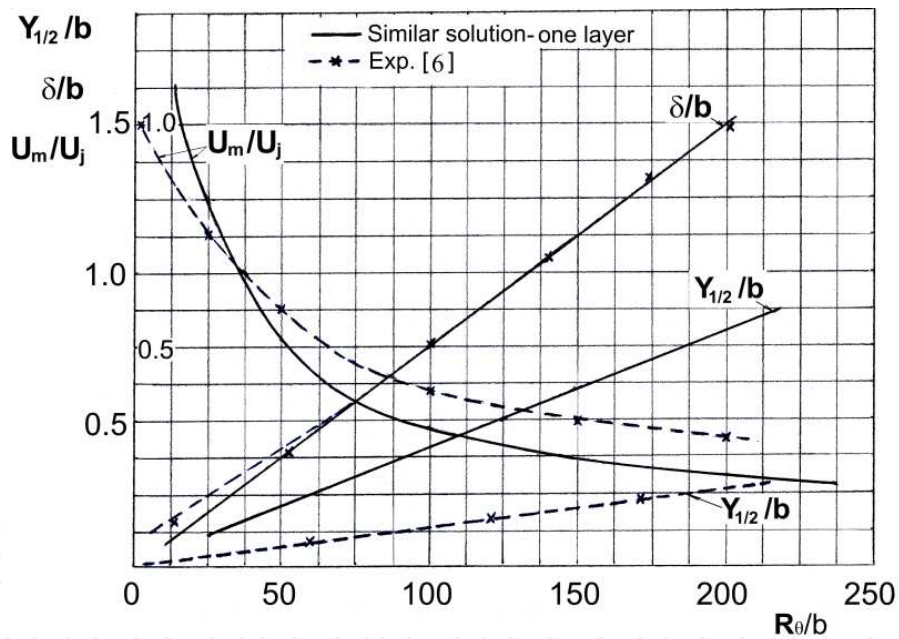


Figure 4. Governing laws for the wall jet flow.

It is easily seen that there are similar solutions of the motion equations (1), (2) and (3), if  $v_t / \nu$  has the form

$$v_t / \nu = \sigma \theta^c. \tag{31}$$

In the present model the viscosity does not take into account the outer intermittent flow, so that the assumption of constant value in the cross section leads to velocity profiles identical to those of laminar flows, though the general configuration of the flow development is different. Suppose in this case that a linear flow develops, then the dimensionless coordinate

of equation (4) must be written as  $\eta \sim y^* / \theta$ , which yields  $c = 1/3$ . Since the rate of increase in width is  $dy_{1/2} / dx = 0.075$ , see [6], we obtain  $\sigma = \text{Re} \frac{4 dy_{1/2} / Rd\theta}{3 \eta_{1/2}}$ , which leads to the

estimation  $\sigma \cong \frac{\text{Re} f_\infty}{148}$  (from the condition  $\frac{V_\theta}{V_{\theta m}} = \frac{f'}{f'_{\max}} = 0.5$  it follows that  $F = 0.90396$  which is used to compute  $\eta f_\infty \cong 14.8$ ). With these data we can now specify the development of the considered self-modelled flow (Figure 4):

- velocity components

$$V_r^* = -\theta^{-2/3} / 3 [f - 3\eta f'], \quad (32)$$

$$V_\theta^* = \frac{4 \text{Re}}{3 \sigma} f' \theta^{-2/3}; \quad (33)$$

- position of virtual origin from the slot

$$\theta_0 = \frac{296 b}{27 R}; \quad (34)$$

- curvature parameter

$$f_\infty = \frac{3}{2.37^{1/3}} \left( \frac{b}{R} \right)^{2/3}; \quad (35)$$

- entrainment parameter

$$A = \frac{f_\infty}{3} \theta^{-2/3}; \quad (36)$$

- augmentation factor of thrust

$$T = \left( \frac{\theta_0}{\theta_1} \right)^{1/3} \left[ 1 - \frac{1}{2} \frac{b \theta_1}{R \theta_0} \right] < 1 \quad (37)$$

- finite thickness of jet sheet, defined as the value for which  $V_\theta = V_{\theta \max} / 2$ . For  $\frac{V_\theta}{V_{\theta m}} = \frac{f'}{f'_{\max}} = 0.5$ , it follows that  $F = 0.90396$  and  $\eta f_\infty \cong 14.8$ . Substituting in (4) we obtain the final result

$$y_{1/2}^* = 0.075 \theta \quad (V_\theta = V_{\theta \max} / 2); \quad (38)$$

- decrease in the maximum flow velocity

$$\frac{V_{\theta m}}{U_j} = \left( 18.5 \frac{b}{\theta R} \right)^{2/3}; \quad (39)$$

- power laws for the wall jet flow

$$y_{1/2}^* \sim x, \quad V_{\theta m}^* \sim x^{-2/3}, \quad x = R\theta. \quad (40)$$

In many applications that use boundary layer control by tangential blowing, the solid surface downstream of the blowing slot is strongly curved and, in this case, the prediction of the jet involves separation and a more accurate knowledge of the flow (radial and tangential pressure - velocity profiles) which can be done with CFD methods.

### 3. Control of the two-dimensional turbulent wall jet on a Coanda surface

Flow control refers to the ability to alter flows with the aim of achieving a desired effect. Examples include the delay of boundary layer separation and drag reduction, noise attenuation, improved mixing or increased combustion efficiency, among many other industrial applications. There are two possibilities to approach the problem of flow separation control: (1) passive control (vortex generators, flaps/slats, slots, absorbant surfaces and riblets) and (2) active control (mobile surface, planform control, jets, advanced controls - magnetodynamics).

The active control without additional net mass flow can be achieved by synthetic jets or small vibrating flap. A synthetic jet is a concept that consists of an orifice or neck driven by an acoustic source in a cavity, as in [10]. At sufficiently high levels of excitation by the acoustic source, a mean stream of flow has been observed to emanate from the neck. The excitation cycle increases the ability of the boundary layer to resist separation.

Another technique of flow control on the convex surfaces is to use passive devices, one of these being the slot mounted between lower-pressure and high-pressure points (near the separation point) on the upper surface. The tendency of equalization of the pressure will produce blowing-suction jets which maintain the boundary layer attached to the upper surface, see [11].

We investigate three issues related to flow control with applications to aerospace and wind energy: finding the appropriate turbulence model for the study of jets on convex surfaces, the passive control using a slot and the active control using a synthetic jet at medium frequencies on Coanda surfaces [12].

#### 3.1. Coanda effect. Computational analysis

In this section the effect of the surface curvature (Coanda effect) on the development of a two-dimensional wall jet is numerically investigated. The main goals are providing a systematic survey of the performance of selected eddy-viscosity models in a range of curved flows and establishing more clearly their potential and limitations.

Reynolds averaged Navier-Stokes simulations (RANS) with different turbulence models have been employed in order to compute the two-dimensional turbulent wall jet flowing around a circular cylinder: (1) Spalart and Allmaras (SA - one turbulence model equation) [13], (2) Launder and Spalding  $k-\varepsilon$  model [14], (3) Wilcox  $k-\omega$  model [15] and (4) Menter  $k-\omega$  SST model [16]. The predictions yielded by the simulations were compared to available experimental measurements from the literature. The surface curvature enhances the near-wall shear production of turbulent stresses and is responsible for the entrainment of the ambient fluid which causes the jet to adhere to the curved surface.

The particular configuration shown in Figure 5 is considered cylindrical. The wall jet properties have been reported by Neuendorf and Wygnanski [17] and provide the means to evaluate the simulation results (diameter  $d = 2R = 0.2032$  m, nozzle height  $b = 2.34$  mm and jet-exit velocity  $U_j = 48$  m/s).

The computational grid used for these investigations consists of  $900 \times 220$  nodes. For the turbulence models used in these calculations the laminar sublayer needed to be resolved. The  $y^+$  values of the wall-next grid points were between 0.4 and 1, and the  $\Delta x^+$  values were between 50 and 300. The grid resolution in the jet was between 40 and 180 times the local Kolmogorov length scale. A fully developed channel velocity profile was prescribed at the nozzle inflow (no near field), with a medium turbulence. The ambient was quiescent.

For some of these turbulence models the jet-velocity decay and jet-half-thickness versus the streamwise angle are plotted in Figure 6. The jet-half-thickness ( $y_{1/2}$ ) represents the thickness where the jet velocity ( $U_j$ ) is half of the maximum jet velocity ( $U_m$ ) through the same section.

When the  $k-\omega$  model was used in combination with the  $k-\omega$  SST model, a close match of the jet-velocity decay with the measured data was achieved. However, even with this model, the downstream development of the jet-half-thickness was poorly predicted.

The shape of the normalized velocity profiles is best predicted by the  $k-\varepsilon$  model (see Figure 7). Since the predicted half-thickness ( $y_{1/2}$ ) is small for all models, the normalized velocity profiles do not match the experimental velocity profiles neither in the mild pressure region, nor in the adverse pressure region.

For the  $k-\omega$  SST model, the separation location was slightly closer to the experimental data. When the  $k-\varepsilon$  and Spalart-Allmaras models were used, the jet remained attached to the cylinder for more than 260 degrees (see Figure 8).

One weakness of the eddy-viscosity models is that these models are insensitive to streamline curvature and system rotation. Based on the work of Spalart and Shur [18] a modification of the production term has been derived, which allows the  $k-\omega$  SST model to sensitize to the curvature effect.

The results obtained with the corrected (curvature correction - *c.c.*)  $k-\omega$  SST turbulence model were presented in Figures 6, 7 and 8, respectively. The results are close to the experimental data up to about 120 degrees. For larger values, the development of the jet was poorly predicted.

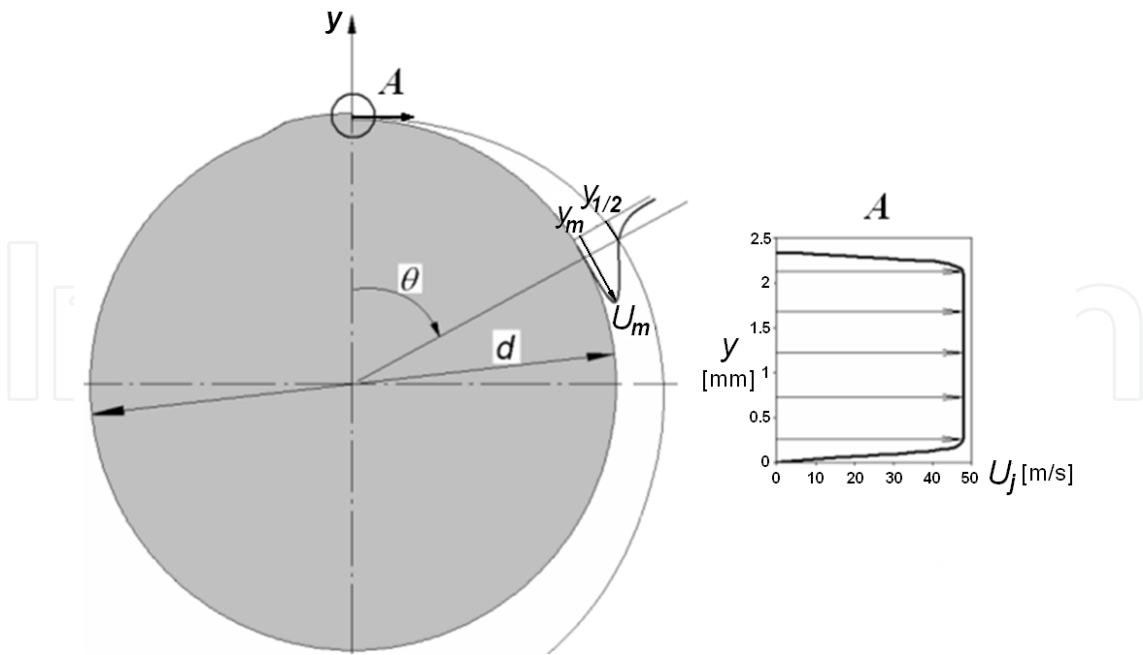


Figure 5. Configuration used in analysis.

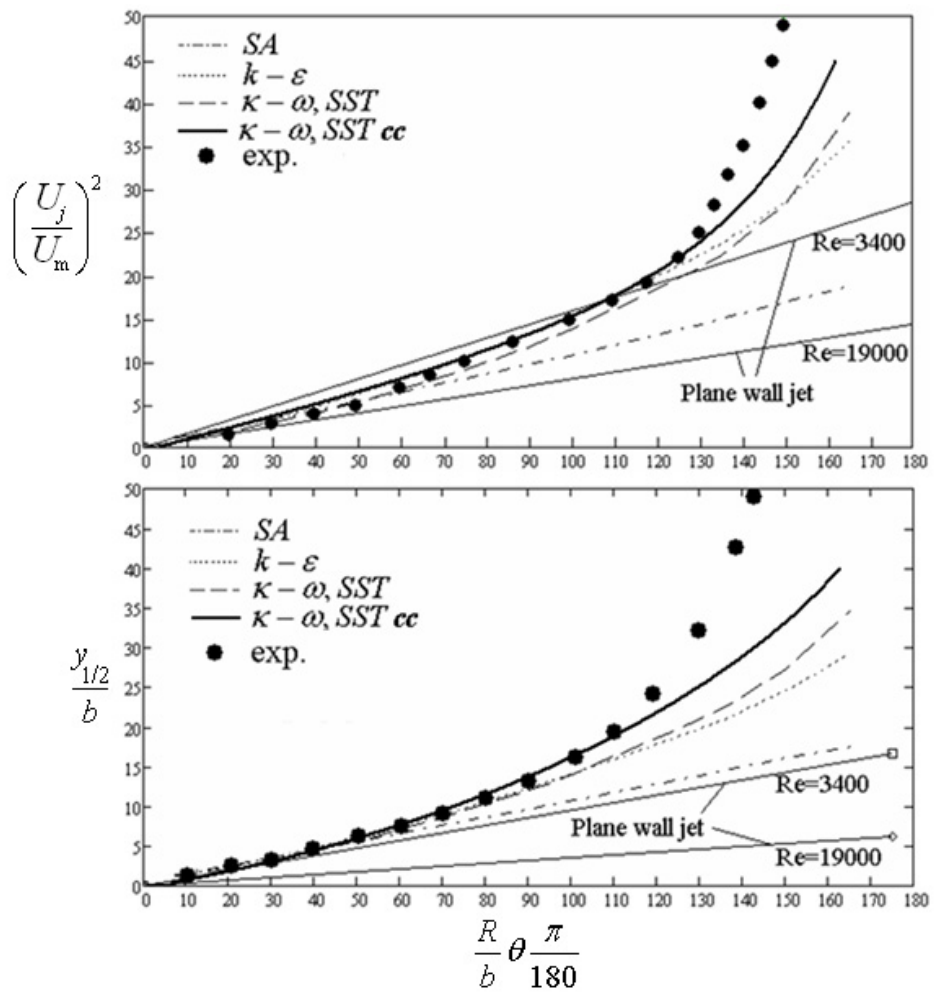


Figure 6. Jet velocity decay and jet-half-thickness (Exp.-Ref.[17]).

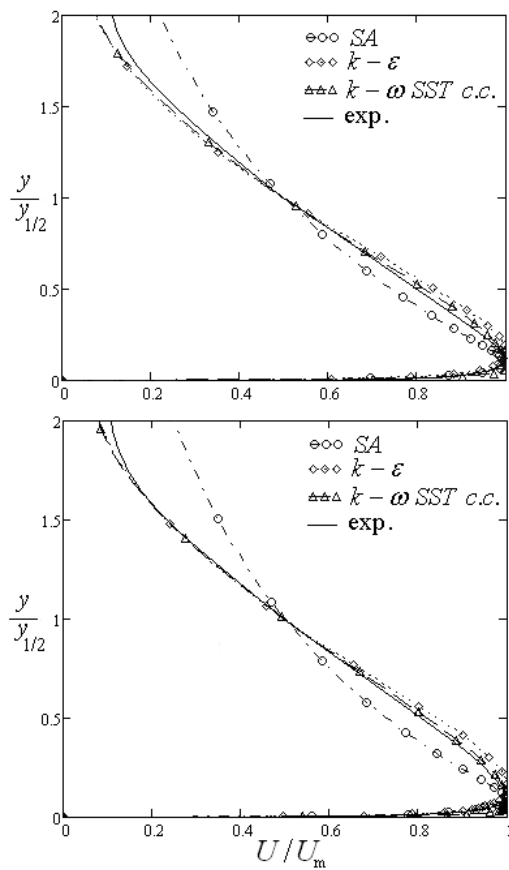


Figure 7. The shape of normalized velocity profiles at  $90^\circ$  and  $180^\circ$  [ $y/y_{1/2}=f(U/U_m)$ ].

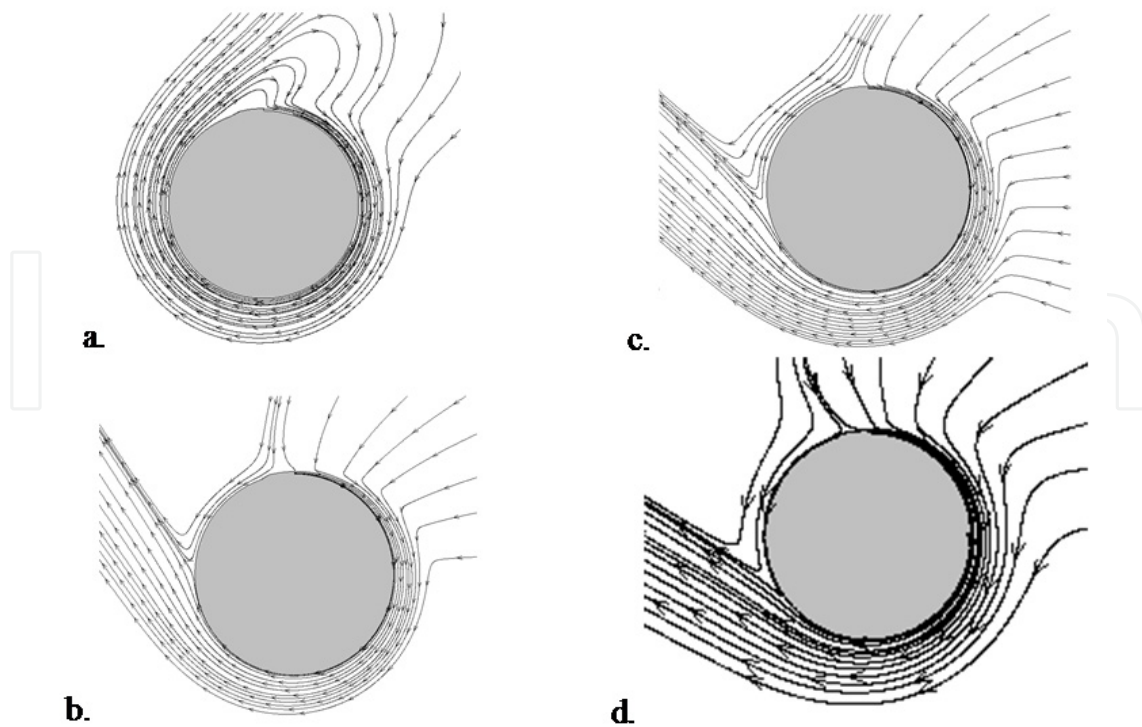


Figure 8. Streamline function: (a) Spalart-Allmaras turbulence model, (b)  $k-\epsilon$  model (enhanced wall option), (c)  $k-\omega$  SST model and (d)  $k-\omega$  SST c.c. model.

### 3.2. Passive control using a slot

The first case study uses a simple convex surface and the second computational case uses the same convex surface with a slot between the over-pressure point and the under-pressure point on the surface (placed in separation boundary layer region). The tendency of equalizing the pressures leads to a blow in the first orifice of the slot, while in the second one the suction phenomenon occurs. The jet ( $U_j=25$  m/s) is developed in a rectangular channel with 75 mm (height)  $\times$  20 cm (width) and passes over a convex surface (25 cm length). The shape of the surface is given by two elliptical fillet surfaces.

The experimental model has 11 pressure probes disposed on the median plane of the Coanda surface and connected to a digital pressure scanner.

For computations we use steady RANS with a  $k-\omega$  SST *c.c.* turbulence model and the computation grid has 219,300 nodes. The suction-blowing phenomenon has a beneficial effect on keeping the boundary layer attached on 82% of the surface compared to the case without the slot when the boundary layer is attached to 58% of the surface. Figure 9 shows the velocity field in the computational domain and the pressure distribution on the surface for each of the aforementioned situations. The jet is deflected by 20 degrees from the original direction. Using a hydraulic resistance on the slot we can control the separation point of the jet and the jet orientation (the problem will be investigated in future work).

For an active control using synthetic jet concept [19], we use the same configuration as in the first case, but the configuration has an actuator with a lateral slot placed at the point of the detached boundary layer. The diaphragm oscillates in a sinusoidal way, with a frequency of 100 Hz and amplitude of 1 mm ( $F^+ = fL/U_j = 1$ ). For simulation purposes, an unsteady RANS,  $k-\omega$  SST turbulence model with curvature correction is used [20]. The computation grid has 160,000 nodes and the  $y^+$  values of the wall-next grid points are between 0.05 and 1, and the  $\Delta x^+$  values between 10 and 100. In this investigation the separation was not completely suppressed and the boundary layer was not enough energized by the generated vortices structures (see Figure 10). A small unsteady deviation on the jet of about 3 degrees was noticed (see Figure 11).

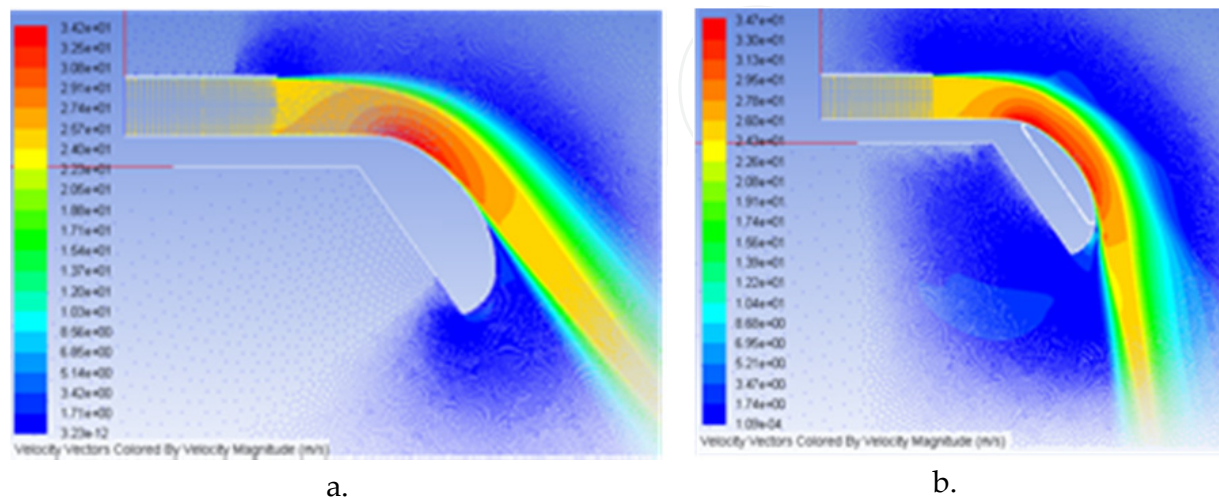


**Figure 9.** Velocity vectors without (a) and with (b) slot.

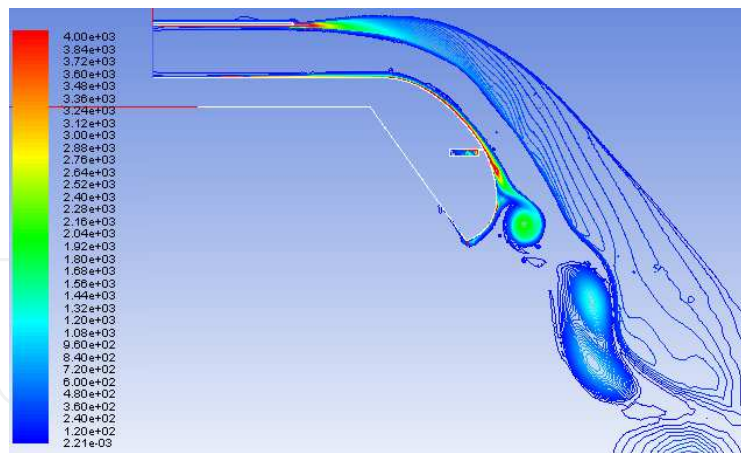


**Figure 10.** Contours of vorticity magnitudes (maximum expulsion).

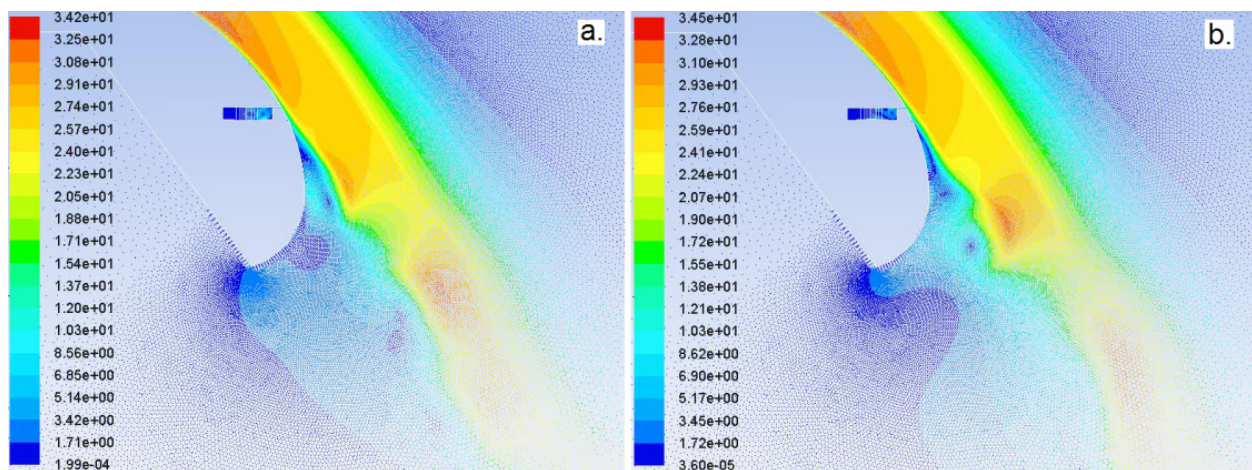


**Figure 11.** Velocity vectors at maximum ingestion (a), and maximum expulsion (b).

#### 4. Numerical analysis of turbulent flow in a Coanda ejector

The task of this study is to investigate the influence of various geometric parameters and pressure ratios on the Coanda ejector performance.

The Coanda ejector is an axisymmetric device that uses the injected primary flow on the inner curved surface and entrains the secondary flow. The main purpose of the Coanda ejector is to provide a high ratio of the induced mass flow rate to the primary mass flow rate. A primary flow is supplied from a high pressure reservoir. The primary flow follows the curved contour of the ejector after a sonic throat, due to the Coanda effect, and expansion waves/compression waves are created depending on the pressure at the outlet section of the primary nozzle. The turbulent mixing of the primary flow with the ambient air near the entrance of the ejector transfers the momentum of the primary jet to the stagnant air in the ejector throat. The secondary, or induced flow is thus dragged by the turbulent shear stress along the viscous effects towards the ejector exit while being mixed with the primary flow by the persistence of a large turbulent intensity throughout the ejector. There are a few works [21, 22, 23] which examine the basic mechanism by which the secondary flow is induced by the ejector.

## 4.1. Mathematical model

**Dimensionless Forms of Fluid Transport Equations.** The fluid transport equations such as the mass (continuity), momentum, and energy conservation equations are used. We define:  $\rho_c$ , the characteristic (inlet) density of the fluid ( $\text{kg/m}^3$ ),  $U$ , the characteristic (inlet) velocity of the fluid (m/s),  $t_c$ , the characteristic time (s), and  $L$ , the characteristic length, which is equal to the inlet diameter of ejector (m) [23, 24].

Then each term is converted to its dimensionless form by multiplying and dividing each term by their characteristic parameters, and then rearranging the equation to the dimensionless parameters. Since the geometrical configuration of the ejector is axisymmetric, the continuity equation and the momentum conservation equation have been used in axisymmetric coordinates.

In compressible fluids, the energy equation is used together with the transport equations in order to calculate fluid properties.

The equations can be spatially averaged to decrease computational cost, yet the averaging process yields a system with more unknowns than equations. Hence, the unclosed system requires a model (e.g., turbulence, or subgrid scale) to make the problem well posed.

**Turbulence Closure Equations.** The basic idea behind the SST model (see [16]) is to retain the robust and accurate formulation of the Wilcox model in the near wall region, and to take advantage of the free stream independence of the model in the outer part of the boundary layer. In order to achieve this, the  $k - \varepsilon$  model is transformed into a  $k - \omega$  formulation by means of a function that has the value one in the near wall region and zero away from the surface. The final form, the model parameters and the implementation are presented in detail in paper [16].

All the equations stated above are used to calculate fluid properties in a CFD code.

## 4.2. Numerical model and results

A numerical model of axisymmetric Coanda ejectors (Fig. 12a) have been built using the CFD software Fluent with a preprocessor, Gambit. The grid size was optimized to be small enough to ensure that the CFD flow results are virtually independent of the size, see [25]. The used grid is divided in a structured grid near the wall and an unstructured grid otherwise. The numerical results have been obtained for a total pressure value of 5 bar, imposed at the reservoir inlet. The computational domain includes the adjacent regions of the ejector with the physical opening boundaries condition. The flow is considered to be steady. We have used the following geometrical configurations (Fig. 12b):  $e_1 = 0.25$  mm,  $R_1 = 7.5$  mm;  $e_2 = 0.4$  mm,  $R_2 = 37.5$  mm .

Figures 13a and 13b show the velocity vectors and the Mach number contours for the investigated axisymmetric Coanda ejector. The induced flow does not follow the path defined by the primary jet. The Mach contours clearly show the flow patterns of the primary and the induced flows and how they mix in the divergent portion of the ejector.

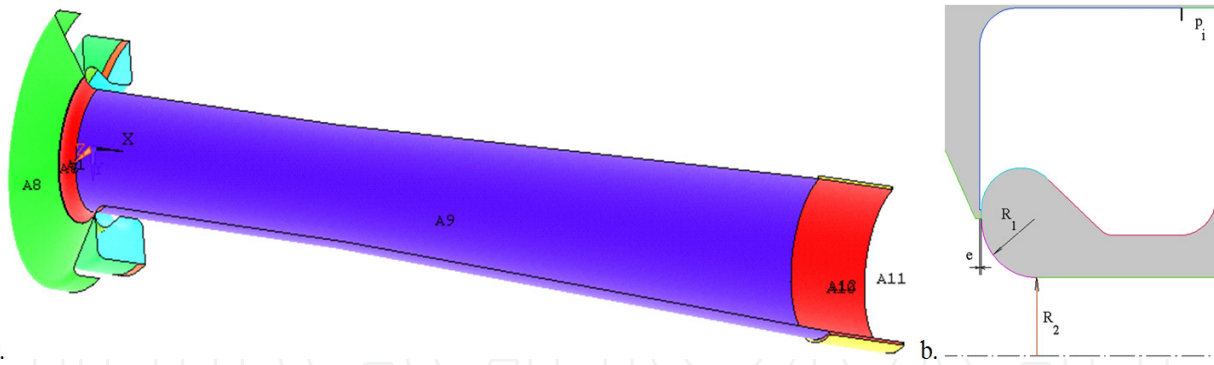


Figure 12. a) Geometry of the Coanda ejector 3D view ; b) detail of the throat gap (primary nozzle).

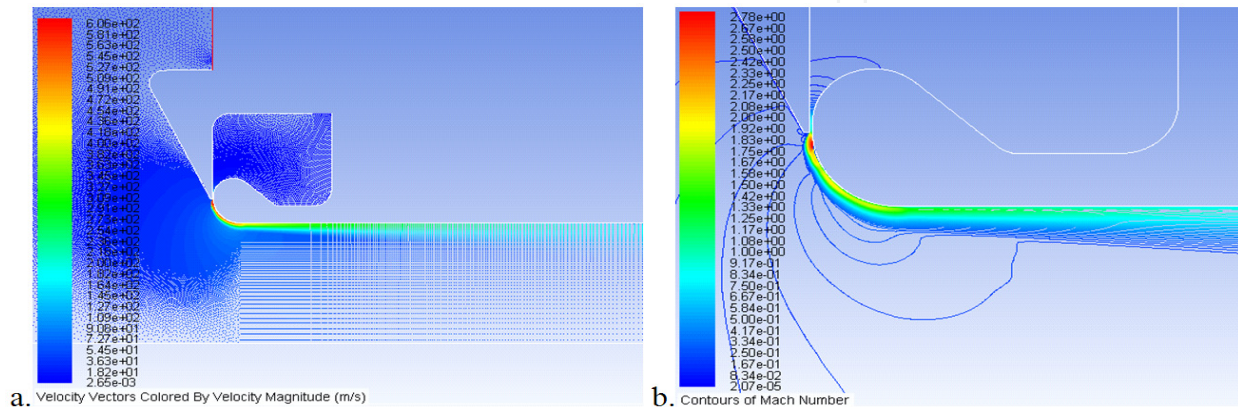


Figure 13. a) Velocity vectors; b) Mach number contour.

In Figures 14a and 14b the flow velocities at  $x = 0$ , and  $x = 550$  are plotted versus the diameters of the Coanda ejector for various values of  $e$ . Note that the graph can be split into two parts: the first part characterized by a large velocity gradient with high velocities (the primary flow) and a second part (the induced flow) where the velocity gradient is small. The flat portion of the velocity profile indicates a mixed flow.

Also the flow velocities for two diameters of the Coanda ejector are analysed. Although cross sectional area increases when the diameter increases, the increment in mass flow rate is quite small.

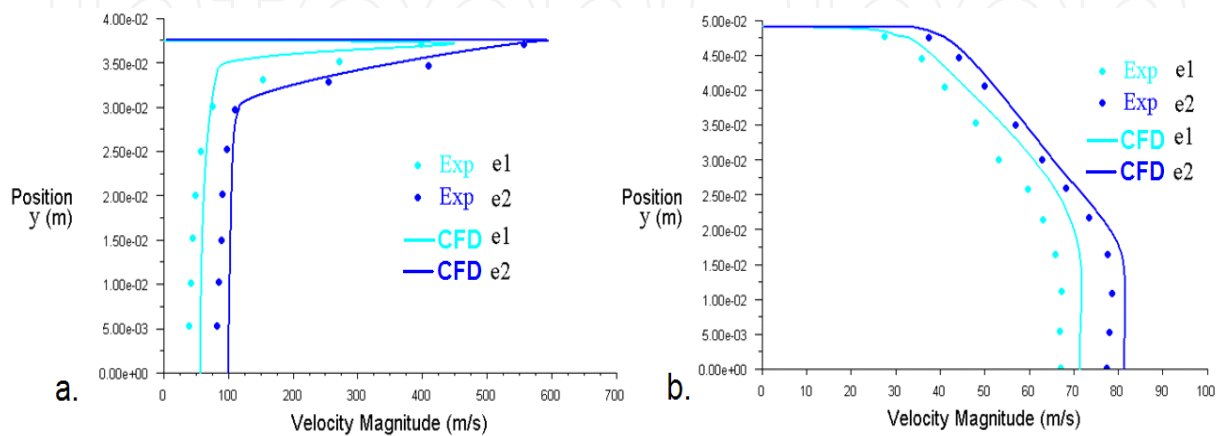


Figure 14. a) Velocity profiles at  $x = 0$ , and b) at  $x = 0.55$  m - b

The optimization study of the Coanda ejector is attempted mainly based on the primary nozzle throat and the stagnation pressure ratio. Based on the computational results, it is seen that the throat gap and the stagnation pressure ratio are the two critical parameters which have great influence on the flow characteristics through the ejector and then on the performance of the Coanda ejector, see [24]. Based on these studies, the optimal configuration of a Coanda ejector might be obtained, in order to maximize the ratio of the mass flow rates.

By performing a computational study the effect of various geometric parameters on the performance of the Coanda ejector has been analyzed. The throat gap of the primary nozzle ( $e$ ) has a strong influence on the ratio of mass flow rates of the induced flow and the primary flow and a critical control over the mixing length as well. For reduced throat gaps, the mixing length decreased, and this possibly indicates the rapid mixing layer growth in the ejector. The mixing layer was more developed for higher values of the diameters of the ejector throat. Validity limits of the calculation laws used in the numerical code have been confirmed by comparisons between numerical and experimental data. The present computational study has allowed us to identify the important parameters which have a strong influence on the behavior and performance of the Coanda ejector.

Further investigations are needed on the primary jet stability and its influence on the flow in the mixing area.

## 5. The pitchfork bifurcation flow in a symmetric 2D channel with contraction

An important application is the study of the incompressible flow in a symmetric 2D channel with contraction.

Experimental and numerical research (see the works [26 – 32]) were performed in order to evaluate the flow through the 2D channel, especially after contraction occurs. The experiments done by Cherdron and Sobey (see [27], [28]) show the preferential formation of a recirculating zone on one of the channel walls, at a given Reynolds number. For values larger than the critical value  $Re_{cr}$ , the flow through the channel loses its symmetry with respect to the channel symmetry axis. This phenomenon is known as pitchfork bifurcation. Physically, in the fluid, a momentum transfer process occurs, causing the appearance of a pressure gradient across the channel. Such a pressure gradient may lead to an asymmetric flow. We refer to this phenomenon as the Coanda effect.

### 5.1. Physical model

The flow equations through the channel are characterized by the Navier-Stokes equations for a laminar, incompressible, stationary flow, given by

$$\begin{aligned}\nabla \vec{V} &= 0 \\ \rho(\vec{V} \cdot \nabla) \vec{V} &= -\nabla p + \mu \nabla^2 \vec{V}\end{aligned}\tag{41}$$

The geometry of the channel is shown in Figure 15 and it has a symmetry axis ( $y = 0$ ). The contraction of the channel is given by the contraction ratio  $k = D/d$ . The inflow of the channel is at a coordinate  $x = -L_1$  with respect to the contraction section, and has the following velocity profile

$$u(y) = 6 V_{med} \left[ 0.25 - (y/D)^2 \right] \quad (42)$$

where  $V_{med} = \frac{1}{D} \int_{-D/2}^{D/2} u(y) dy$ .

The Reynolds number is defined by the mean value of the velocity  $V_{med}$  and the maximum value of the height of the channel  $D$ , i.e.,  $Re = \rho V_{med} D / \mu$ , where  $\rho$  is the fluid (air) density and  $\mu$  is the dynamical viscosity.

The outflow ( $x = L_2$ ) is chosen sufficiently far from the contraction section, such that the velocity gradient associated with the velocity profile is zero ("outflow" output condition).

On the solid boundaries (the walls of the channel) we impose a "no slip" condition. If, for numerical simulations, a half-channel is used, then the presence of the symmetry axis is imposed assuming a zero flux of all quantities across a symmetry boundary.

## 5.2. Numerical model

The "pressure-based" solver that is used has a SIMPLE-C algorithm implemented (see [33]), together with a multi grid technique for increasing the rate of convergence of stationary flow problems (Ansys Fluent). The spatial discretization is of second order accuracy, with a under-relaxation coefficient of 0.5 for both the pressure and the momentum. The solution has converged when the global  $L^2$  - norm of the pressure and the velocity residuals is lower than  $10^{-8}$ .

The Reynolds number sets were selected such that the flow in channel is laminar and stationary.

## 5.3. Numerical results

In the numerical simulations we use three channels with the contraction coefficients  $k = 2.4$  and 8, respectively (see Table 1, and Figure 15). The fixed dimensions of the channel are  $D = 0.2$  m,  $L_1 = 0.5$  m and  $L_2 = 1$  m.

$k$	$d = D/k$ (m)	Re	$\Delta s = \min(\Delta x, \Delta y)/D$	Grid nodes (full channel)
2	0.1	500...3600	2.50e-4	413,400
4	0.05	500...2000	1.25e-4	415,990
8	0.025	400...1700	1.00e-5	433,800

**Table 1.** Computation settings.

The recirculation zones that occur at the corners of the channel and beyond the contraction section have the lengths  $S_1$ ,  $S_2$ , and  $S_3^l$ ,  $S_3^u$ , respectively (see Figure 15).

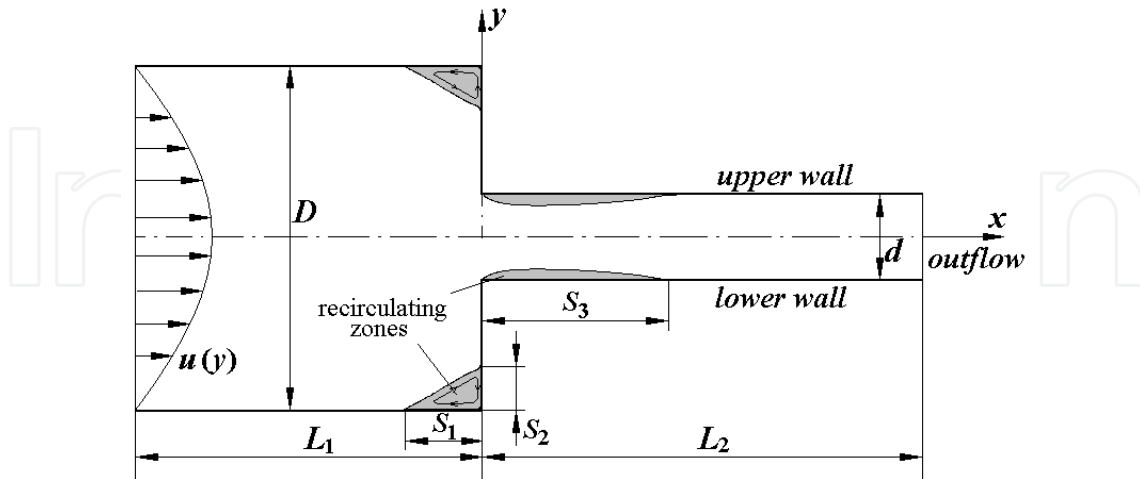


**Figure 15.** The geometry and the reference lengths that characterize the recirculating zones (near corners and in downstream channel).

For each contraction coefficient  $k$ , two computation cases occur: a first case in which we have used half-channel ( $y = 0$  is a symmetry boundary) and a second case in which the flow through the whole channel has been studied. The computational domain allows for generating orthogonal grids.

For a given value of  $k$ , without changing the value of the Reynolds number, the numerical simulations lead to similar values of the length(s) of the recirculation zone ( $S_1$  and  $S_2$ ) in the corner(s) of the upstream channel, in accordance with the results from the works of Hawken [30]. The relative error between the simulated values  $S_1$  and  $S_2$  (whole channel, upper and lower corner) and the values obtained from the half-channel simulations is under 1% (see Figure 16).

Figure 17 shows that, for the half-channel symmetric solution, the reattachment length  $S_3$  is linear and monotonously increasing.

Concerning the full channel solution we make the following remarks:

- the use of a grid which is symmetric with respect to the symmetry axis of the channel and has symmetrically generated grid computing boundaries usually leads to a symmetric solution (see Figure 17b);
- if the grid is slightly asymmetric (the values of the symmetric coordinates are slightly perturbed or the number of discretization points is different for each symmetric boundary) or if the initial flow field is slightly perturbed, then the recirculation zone formed on the lower wall is different from the recirculation zone formed on the upper wall ( $S_3^l \neq S_3^u$ ) (see Figure 17c). The results hereby have been obtained using four layers of cells, in the neighborhood of the lower wall, each cell splitted into two parts (keeping  $\Delta y$  and keeping the grid orthogonal).

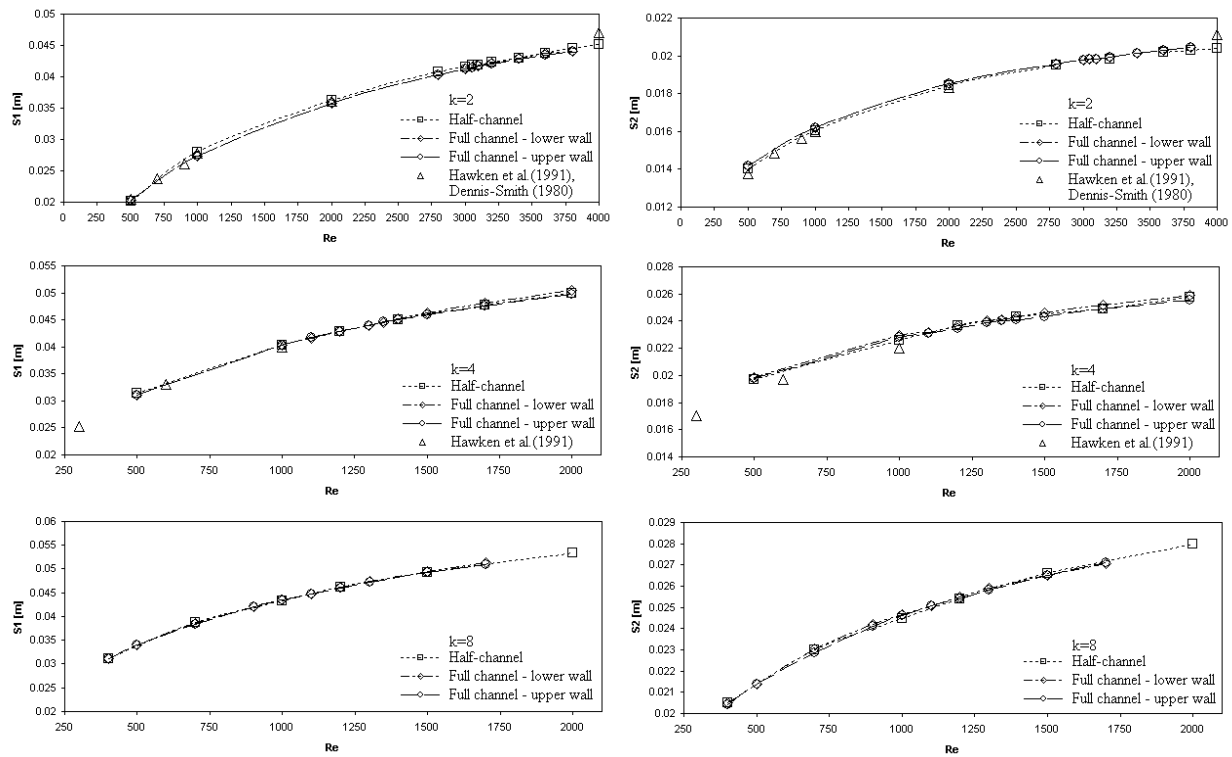


**Figure 16.** The computed separation ( $S_1$ ) and reattachment lengths ( $S_2$ ) for computed symmetric solution in a half-channel and full channel (lower and upper corner).

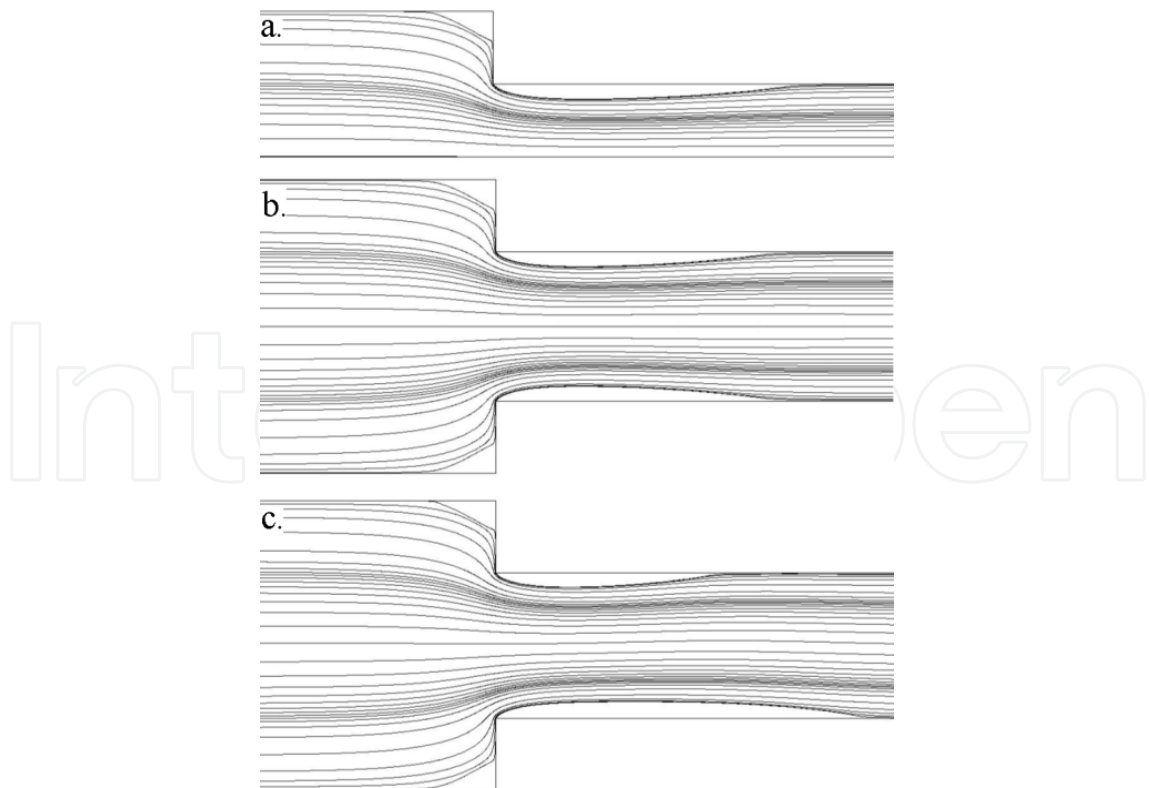


**Figure 17.** Pathlines for  $k=2$  and  $Re=3600$ : (a) half-channel, (b) full-channel symmetric mesh and (c) full-channel with asymmetric orthogonal mesh.

Figure 18 shows the evolution of the reattachment length  $S_3$  for both half-channel and full channel solutions, on the lower wall of downstream channel ( $S_3^l$ ) and on the upper wall ( $S_3^u$ ) respectively. Note that up to a certain value of the Reynolds number the full channel numerical solution is identical to the half-channel numerical solution (the relative error is under 1%). For values greater than the aforementioned Reynolds number, a longer recirculation zone occurs on one of the walls of the channel, e.g., the lower wall, in our case. The critical value of the Reynolds number that leads to the bifurcation of the solution lies in the range: (1)  $3050 < Re_{cr} < 3100$  for  $k = 2$ , (2)  $1350 < Re_{cr} < 1400$  for  $k = 4$  and (3)  $1050 < Re_{cr} \approx 1100 < 1150$  for  $k = 8$ .

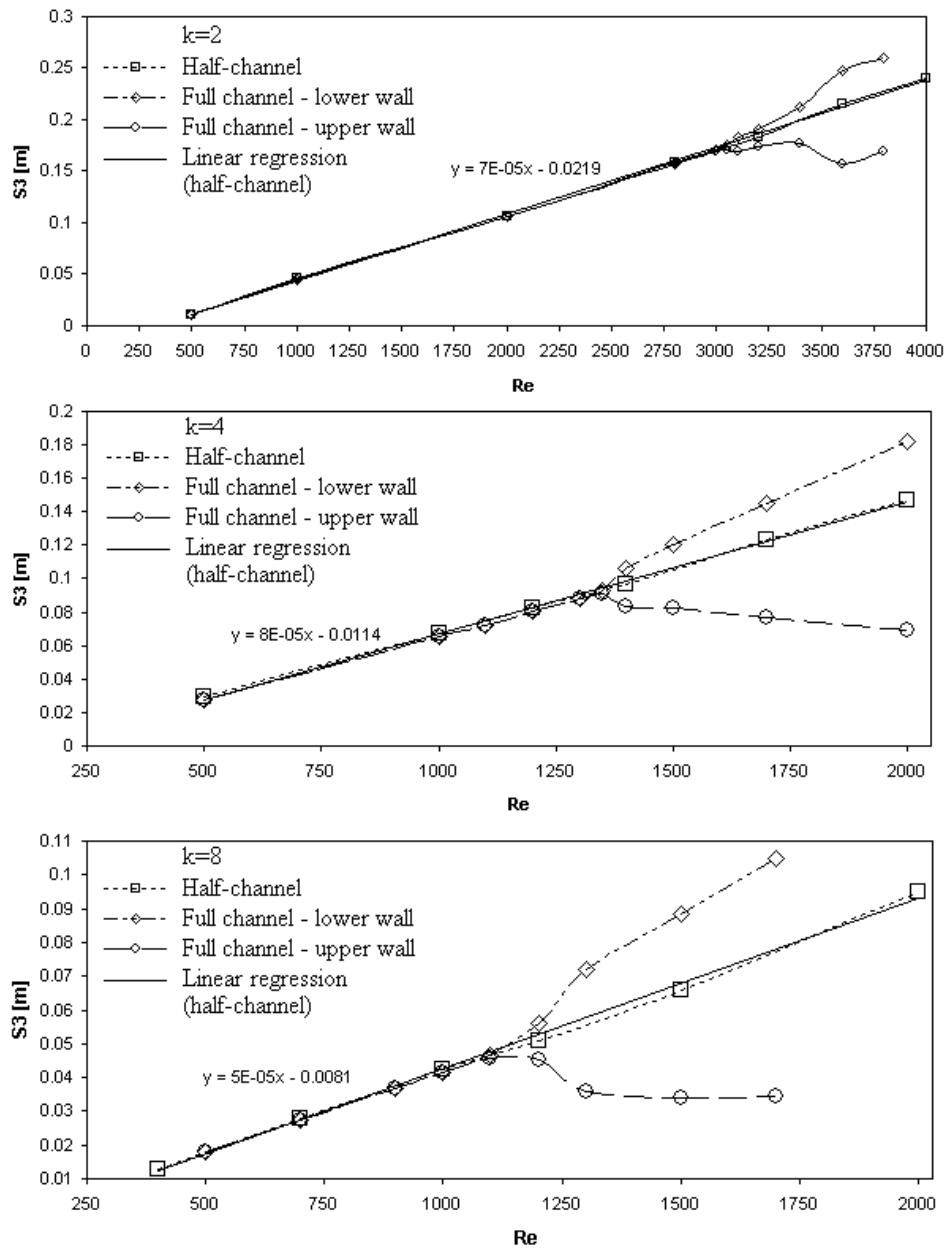


**Figure 18.** The plot of reattachment length  $S_3$  after contracted section (i.e. downstream channel) as a function of Reynolds number .

The numerical simulations confirm the pitchfork bifurcation of the solution. The asymmetric solution given by the two different recirculation zones that occur on the upper and lower wall, respectively, can be stabilised up to a value of approximately 3800 of the Reynolds number for  $k = 2$ , 2000 for  $k = 4$  and 1700 for  $k = 8$ , respectively.

Another application where the pitchfork bifurcation occurs is the study of two flows that go through a channel [34]. We consider the case when the velocity profile is described by equation (42), and assume that the flows have identical velocity profiles (see Figure 19). The flowing regime is characterized by small Reynolds numbers ( $< 25-30$ ) such that the flows are laminar and stationary. The domain is discretized in  $400 \times 600$  nodes [35]. When the Reynolds number ( $Re = \rho V_{med} D / \mu$ ) is larger than the critical value  $Re_{cr}$  the symmetry of the flow is lost, hence the flow becomes asymmetric. Figure 20 shows the flow patterns for  $S/D = 10$ ,  $S/H = 0.4$  and  $L/H = 15$ , for  $Re = 15, 19$  and  $24$ , respectively. In Figure 20.b the jets unite into a single jet deflected towards one side-wall, which is then redirected to the opposite side-wall downstream. According to Figure 20.c the number of separation bubbles increase with the  $Re$  number, and the flow becomes unsteady.

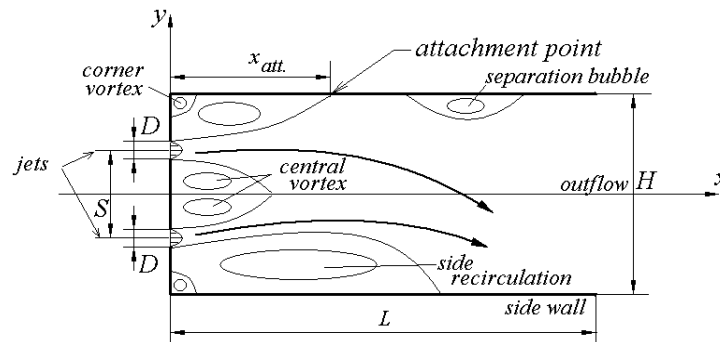


**Figure 19.** Twin-jet flow configuration.

Figure 21 shows the attachment point locations  $x_{att}$  for flows at various Reynolds numbers, for fixed ratio  $S/D = 10$ . This point apparently remains unchanged for  $S/H < 0.5$ , since the core region between jets is distant from side-walls and the walls do not influence it. For  $S/H \geq 0.5$ , the walls are relatively closer to the jets, and the Coanda effects lead to the “attraction” of jets towards the walls with the merging point suddenly jumping to a further downstream location (observed for  $Re > 15$ ).

The transonic airfoil buffet [36, 37] is a stability issue that leads to shock oscillations and large variations of the lift coefficient. The practical problem of the airplane buffet is given by the dynamic response of the elastic structure at the flow field [38].

The prediction of the onset and character of the unsteady transonic flow field is a great challenge. The transonic flow around an airfoil has been used as a model problem for understanding the unsteady forcing, phenomenon similar to airplane buffeting [39].

Many researchers analyze the problem using the Reynolds-averaged Navier–Stokes equations with adequate turbulence closure, which are a necessary approximation to cover the high Reynolds numbers at which transonic buffet occurs.

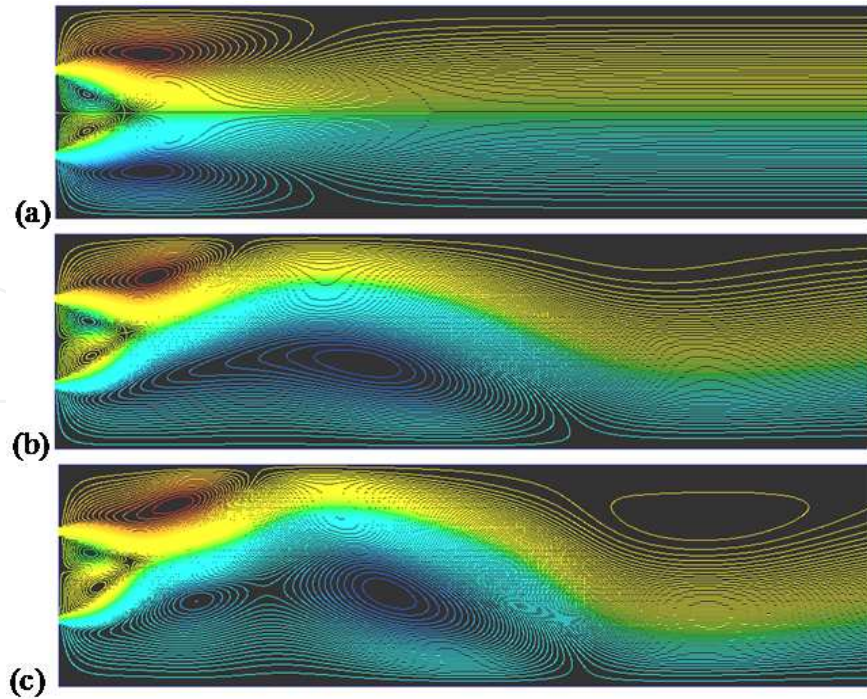


Figure 20. Streamlines for case  $S/D = 10$ ,  $S/H = 0.4$ : (a)  $Re=15$ , (b)  $Re=19$  and (c)  $Re=24$ .

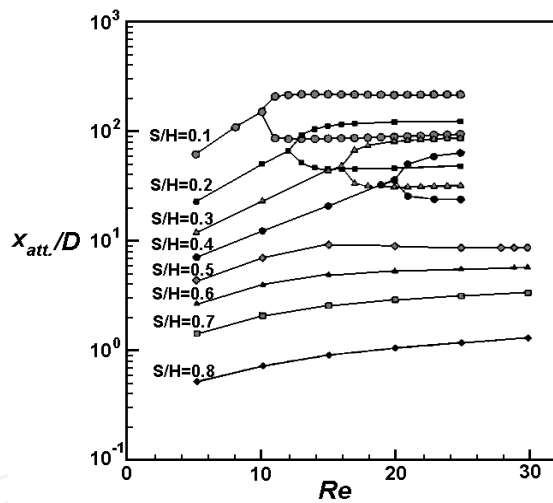
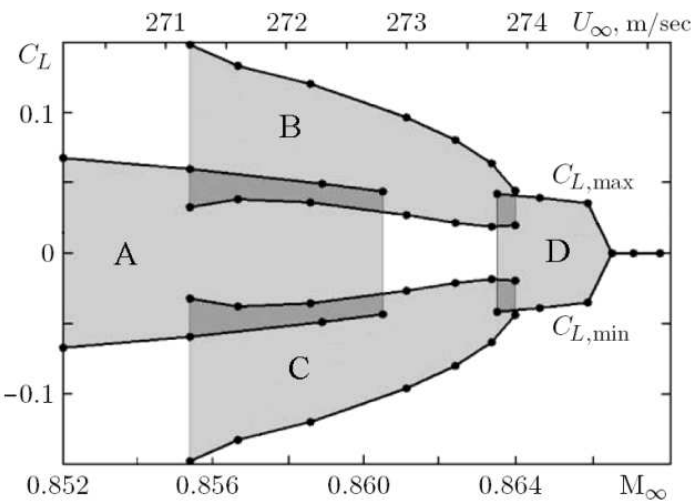


Figure 21. The attachment length for various  $Re$  and  $S/H$  for  $S/D = 10$ .

A simple exemplification for **bifurcation in transonic flow** over an particular airfoil is presented in the following section. The reference model can be found in ref. [40].

In figure 22, for the set of Mach incidence numbers  $0.852 < M_\infty < 0.868$ , one may notice the appearance of the solution bifurcation. The bifurcation is given by the relation  $C_L = f(M_\infty)$ , resulting in four domains with different supersonic flow profiles:

- domains A and D, which correspond to the solution obtained by starting with a uniform flow at an angle of  $0^\circ$ ;
- domains B and C, which correspond to the solution obtained by starting with the initial solution at  $\pm 1^\circ$  and  $M_\infty=0.86$ .



**Figure 22.** Extreme values of the lift coefficient  $C_L$  as function of the Mach number  $M_\infty$  for self-sustained flow oscillations about the particular symmetric airfoil (relative airfoil thickness  $h = 0.09$ ) at  $0^\circ$  incidence and  $Re = 1.1 \times 10^7$ : domains A, B, C and D describes the flow regimes with different location of supersonic regions [40].

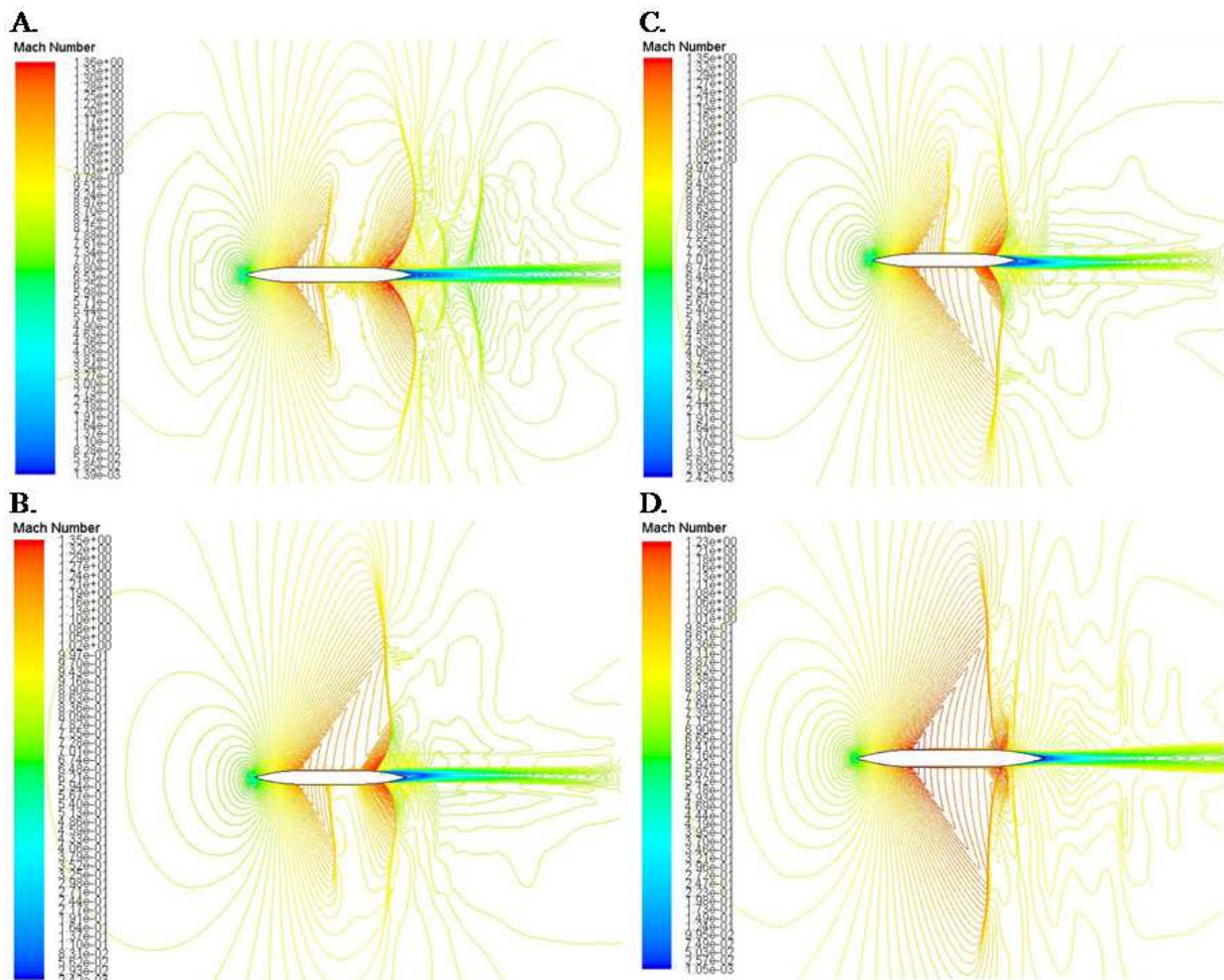


**Figure 23.** (A., B., C., D.) - The flow regimes with different supersonic regions computational domains has 1.1 million cells (hybrid mesh with quadrilateral cells near the airfoil). Solver used: unsteady Reynolds-averaged Navier-Stokes implicit solver with SST  $k-\omega$  turbulence model.

The nonlinear flow equations, the initial solution used for the numeric computations and the length of the airfoil midpart with a small or zero curvature are the principal factors for the onset of flow bifurcations [40, 41].

## 6. Conclusion

In the beginning of the chapter we have achieved an analytic solution that approximates a two-dimensional Coanda flow. The validity of the results is limited to the cases given by  $b/R \ll 1$ , since in the tangential component of momentum equation the curvature was neglected ( $y^* \ll 1$ ).

The validity of the laminar solution is for Reynolds numbers smaller than the critical value which is of the order  $3 \times 10^4$ . For the turbulent flow the similarity assumption has been reduced primarily to the general development along the flow, leaving the transverse distribution of shear stress.

In this model the edge of the intermittent flow has been neglected, so that assuming constant turbulent viscosity in cross section has led to similar velocity profiles for both the laminar and turbulent flow. However, the general configuration of the flow development was different. In order to specify the development of this self-modeled flow only one empirical constant was needed.

In many applications that use boundary layer control by tangential blowing, the solid surface downstream of blowing slot is strongly curved and, in this case, the prediction of jet involves separation and a more accurate knowledge of the flow (radial and tangential pressure - velocity profiles) which has been done by CFD methods.

The compressible Reynolds-averaged Navier–Stokes (RANS) equations have been solved for circulation control (CC) airfoil flows. Different turbulence models have been considered for closure, including the Spalart–Allmaras model with and without a curvature correction and the shear stress transport (SST) model of Menter. Numerical solutions have been computed with a structured grid solver. The effect of mesh density on the solutions has been examined.

We have investigated the characteristics of various Coanda surfaces, involving smooth curved surfaces and a polygonal curved surface with flap. Using the FLUENT code we have analyzed the distribution pressure and separation on the considered surfaces.

Further, we have taken interest in the detailed behavior of an existing Coanda ejector model, used in propulsion systems. For numerical investigations we have used an implicit formulation of RANS equations for axisymmetric flow with a shear stress transport  $k - \omega$  (SST model) turbulence model. The numerical results have been obtained for a total pressure range of 1-5 bars, imposed at the reservoir inlet. The goal was to investigate the influence of various geometric parameters and pressure ratios on the Coanda ejector performance. The effect of various factors, such as the pressure ratio, primary nozzle and ejector configurations on the system performance has been evaluated based on the

performance parameters. The mixing layer growth plays a major role in optimizing the performance of the Coanda ejector as it decides the ratio of secondary mass flow rate to primary mass flow rate and the mixing length.

Because single jet flows or multi-jet flows are extensively applied in conjunction with the Coanda surface, as confined or free jet flows, in the last part of the chapter we have provided further insight into complexities involving issues such as the variety of flow structure and the related bifurcation and flow instabilities.

We have considered two cases: i) the flow bifurcation in the symmetric planar contraction channel for different contraction ratio and Reynolds number (single jet) and ii) the flow structure as bifurcation phenomena involved in the confined twin-jet flow field, related to the parameters of jet momentum ( $Re$ ), side-wall confinement and jet proximity effects.

Also was presented a simple exemplification for bifurcation in transonic flow over an particular airfoil.

Thus, we have determined the conditions and the limits within which one can benefit from the advantages of Coanda-type flows.

## Author details

A. Dumitrache

*Institute of Statistics and Applied Mathematics of the Romanian Academy, Bucharest, Romania*

F. Frunzulica

*Institute of Statistics and Applied Mathematics of the Romanian Academy, Bucharest, Romania  
"POLITEHNICA" University of Bucharest, Faculty of Aerospace Engineering, Bucharest, Romania*

T.C. Ionescu

*Imperial College London, Dept. Electrical and Electronic Eng., Control & Power Group, London, UK*

## 7. References

- [1] Bourque C., Newman BG. Reattachment of a two – dimensional - incompressible jet of an adjacent flat plate. *The Aeronautical Quarterly* 1960; XI part 3 201-232.
- [2] Newman BG. The deflection of plane jets adjacent boundaries – Coanda effect. In: Lachmann GV. (ed.) *Boundary Layer and Flow Control Principles and Applications*, vol. I, New York: Pergamon Press Inc.; 1961. p232-264.
- [3] Kruka V., Eskinazi S. The wall – jet in a moving stream. *Journal of Fluid Mechanics* 1964; 20(4) 555-579.
- [4] Williams JC., Cheng EH., Kim KH. Curvature effects in a laminar and turbulent free jet boundary. *AIAA Journal* 1971; 4 733-736.

- [5] Dumitrescu H., Ion S., Dumitrache A. Similar solutions of a Coanda-type flow. *St. Cerc. Mec. Apl.*, Bucharest, 1988; 47(6), 531-543 (in Romanian).
- [6] Kind RJ. Calculation of the normal – stress distribution in a curved wall jet. *The Aeronautical Journal of the Royal Aeronautical Society* 1971; 343-348.
- [7] Sawyer RA. Two dimensional reattaching jet flow including the effect of curvature on entrainment. *Journal of Fluid Mechanics* 1963; 17 481-498.
- [8] Ljuboja M., Rodi W. Calculation of turbulent wall jets with an algebraic Reynolds stress model. *Journal of Fluids Engineering* 1980; 102(3) 350-356.
- [9] Reynolds AJ. *Curgeri turbulente in tehnica*. Bucuresti: Editura Tehnica; 1982. (in Romanian).
- [10] Slomski JF., Chang PA. Large Eddy Simulation of a Circulation Control Airfoil. *AIAA Paper* 2006-3011 2006.
- [11] Glezer A., Amitay M. Synthetic Jets. *Annu. Rev. Fluid Mech.* 2002; 34 503-529.
- [12] Frunzulica F., Dumitrache A., Preotu O., Dumitrescu H. Control of two-dimensional turbulent wall jet on a Coanda surface. In: Brenn G., Holzapfel G.A., Schanz M., Steinbach O. (eds.) *Proceedings in Applied Mathematics and Mechanics. Special Issue: 82nd Annual Meeting of the International Association of Applied Mathematics and Mechanics (GAMM), Graz 2011: H11(1), H651–652.*
- [13] Spalart PR., Allmaras SR. A one-equation turbulence model for aerodynamic flows. *AIAA Paper* 92-0439 1992.
- [14] Launder BE., Spalding DB. The numerical computation of turbulent flows. *International Journal for Numerical Methods in Fluids* 1974; 15 127-136.
- [15] Wilcox D. Simulation of transition with a two-equation turbulence model. *AIAA Journal* 1994; 32 1192-1199.
- [16] Menter FR. Eddy viscosity transport equations and their relation to the  $k-\omega$  model. *ASME Journal of Fluids Engineering* 1997; 119 876-884.
- [17] Neuendorf R., Wygnanski I. On a turbulent wall jet flowing over a circular cylinder. *Journal of Fluid Mechanics* 1999; 381 1-25.
- [18] Shur ML., Strelets MK., Travin AK., Spalart PR. Turbulence Modeling in Rotating and Curved Channels: Assessing the Spalart-Shur Correction. *AIAA Journal* 2000; 38(5) 784-792.
- [19] Rizzetta DP., Visbal MR., Stanek MJ. Numerical investigation of synthetic jet flowfields. *AIAA Paper* 98-2910 1998.
- [20] Fluent ANSYS 12. User Guide.
- [21] Gregory-Smith DG., Senior P. The effect of base steps and axisymmetry on supersonic jets over Coanda surfaces. *Intl. J. Heat and Fluid Flow* 1994; 15 291-298.
- [22] Guerriero V., Baldas L., Caen R. Numerical solution of compressible flow mixing in Coanda ejectors. In : *Proc. the 8th Symposium on Fluid Control, Measurement and Visualization, 2005, Chengdu, China, 1–7.*
- [23] Kim HD., Lee JH., Segouchi T., Matsuo S. Computational analysis of a variable ejector flow. *Journal of Thermal Science* 2006; 15 140-144.

- [24] Dumitrache A., Frunzulica F., Preotu O., Dumitrescu H. Numerical analysis of turbulent flow in a Coanda ejector. In: Brenn G., Holzapfel G.A., Schanz M., Steinbach O. (eds.) Proceedings in Applied Mathematics and Mechanics. Special Issue: 82nd Annual Meeting of the International Association of Applied Mathematics and Mechanics (GAMM), Graz 2011; H11(1), H647–648.
- [25] Riffat SB., Everitt P. Experimental and CFD Modelling of an Ejector System for Vehicle Air Conditioning. *Journal of the Institute of Energy* 1999; 72(6) 41-47.
- [26] Durst F., Schierholza WF., Wunderlich AM. Experimental and numerical investigations of plane channel flows with sudden contraction. *ASME Journal of Fluids Engineering* 1987; 109 376-383.
- [27] Cherdron W., Durst F., Whitelaw J. Asymmetric flows and instabilities in symmetric channels with sudden expansion. *Journal of Fluid Mechanics* 1978; 84 13-31.
- [28] Sobey IJ. Observation of waves during oscillating channel flow. *Journal of Fluid Mechanics* 1985; 151 395-426.
- [29] Hunt R. The numerical solution of the laminar flow in a constricted channel at moderate high Reynolds number using Newton iteration. *International Journal for Numerical Methods in Fluids*, 1990; 11 247-259.
- [30] Hawken DM., Townsend P., Webster MF. Numerical simulation of viscous flows in channels with a step. *Computers & Fluids* 1991; 20 59-75.
- [31] Dennis SC., Smith FT., Steady flow through a channel with a symmetrical constriction in the form of a step. *Proceedings of the Royal Society, London, Series A372* 393-414.
- [32] Drikakis D. Bifurcation in phenomena in incompressible sudden expansion flows, *Phys. Fluids* 1997; 9(1) 76-87.
- [33] Van Doormaal JP., Raithby GD. Enhancement of the simple method for predicting incompressible fluid flows. *Numerical Heat Transfer* 1984; 7 147-163.
- [34] Tzeng PY., Soong CY., Hsieh CD. A numerical investigation of side-wall confinement effect on two turbulent parallel plane jets. *J. Chin. Soc. Mech. Eng.* 1988; 19 167-178.
- [35] Govaerts WJF. Numerical methods for bifurcation of dynamical equilibria. Gent: SIAM; 2000.
- [36] Crouch J D., Garbaruk A., Magidov D., Travin A. Origin of transonic buffet on aerofoils. *J. Fluid Mech.* 2009; 628 357-369.
- [37] Xiao Q., Tsai HM., Liu F. Numerical Study of Transonic Buffet on a Supercritical Airfoil. *AIAA Journal* 2006; 44(3) 620-628.
- [38] Awrejcewicz J. Bifurcation and Chaos in Coupled Oscillators. World Scientific, Singapore, 1991.
- [39] Awrejcewicz J., Krysko VA., Nonclassical Thermoelastic Problems in Nonlinear Dynamics of Shells. Springer-Verlag, Berlin 2003.
- [40] Kuz'min G. Bifurcations of transonic flow past simple airfoils with elliptic and wedge-shaped noses. *Journal of Applied Mechanics and Technical Physics* 2010; 51(1) 16–21.

- [41] Ivanova AV. Structural instability of inviscid transonic channel flow. *Journal of Engineering and Thermophysics* 2003; 76(6) 1262-1265.

IntechOpen

IntechOpen